remote sensing

MDPI

Article

Early Detection of Pine Wilt Disease by Combining Pigment and Moisture Content Indices Using UAV-Based Hyperspectral Imagery

Rui Hou [1,2], Biyao Zhang [1,*], Guofei Fang [3,4], Sihan Yang [5], Lei Guo [5], Wenjiang Huang [1,2], Jing Yao [1], Quanjun Jiao [1], Hong Sun [3,4] and Jiayu Yan [3,4]

[1] State Key Laboratory of Remote Sensing and Digital Earth, Aerospace Information Research Institute, Chinese Academy of Sciences, Beijing 100101, China; hourui21@mails.ucas.ac.cn (R.H.); huangwj@aircas.ac.cn (W.H.); jasonyao92@gmail.com (J.Y.); jiaoqj@aircas.ac.cn (Q.J.)
[2] University of Chinese Academy of Sciences, Beijing 100049, China
[3] Center for Biological Disaster Prevention and Control, National Forestry and Grassland Administration, Shenyang 110034, China; fgfly@163.com (G.F.); sunhongcaf@163.com (H.S.); yanjiayu212@163.com (J.Y.)
[4] Key Laboratory of National Forestry and Grassland Administration on Forest and Grassland Pest Monitoring and Warning, Shenyang 110034, China
[5] Beijing Garden Greening Resources Protection Center (Beijing Municipal Bureau of Landscape and Greening Approval Service Center), Beijing 101118, China; bjlinbaozhancbk@yllhj.beijing.gov.cn (S.Y.); guolei@yllhj.beijing.gov.cn (L.G.)
* Correspondence: zhangby@aircas.ac.cn

Abstract: Pine wilt disease (PWD) is characterized by rapid transmission, high mortality rates, and difficulty in control, resulting in severe and destructive impacts on both the ecological environment and socioeconomic development in China. Due to the lack of significant symptoms in infected trees during the early stages of the disease, improving the accuracy of early detection has become a major challenge in PWD monitoring. In recent years, the rapid advancement of UAV-based hyperspectral remote sensing technology has provided a promising approach for the early detection of PWD. In this study, we selected classic canopy pigment and moisture content indices to construct a set of recognition indicators. The optimal canopy pigment index (CI) and canopy moisture content index (WASCOSBNDI) were then chosen through significance testing and derivative analysis. Based on the asynchronous variations in canopy moisture and pigment content during the development of PWD, the CI, WASCOSBNDI, and CI-WASCOSBNDI models were developed using a multi-threshold segmentation method to identify trees at different stages of infection. The results demonstrate that the CI-WASCOSBNDI model achieved the highest accuracy in detecting infection stages, with an overall classification accuracy of 92.78%. In comparison, the CI and WASCOSBNDI models achieved classification accuracies of 81.34% and 89.84%, respectively. For the early stage infected trees, which are the primary focus of this study, the CI-WASCOSBNDI model exhibited the best performance with an accuracy rate exceeding 70%, significantly outperforming the other models. Furthermore, the timing of infection in early stage trees significantly influenced the model's detection accuracy, with trees closer to the disease outbreak period being more easily identified. These findings provide a reference for the accurate early monitoring of PWD using UAV hyperspectral imagery.

Keywords: pine wilt disease; early detection; UAV hyperspectral; pigment index; moisture content index; multi-threshold segmentation

Received: 18 March 2025
Revised: 12 May 2025
Accepted: 22 May 2025
Published: 23 May 2025

Citation: Hou, R.; Zhang, B.; Fang, G.; Yang, S.; Guo, L.; Huang, W.; Yao, J.; Jiao, Q.; Sun, H.; Yan, J. Early Detection of Pine Wilt Disease by Combining Pigment and Moisture Content Indices Using UAV-Based Hyperspectral Imagery. *Remote Sens.* **2025**, *17*, 1833. https://doi.org/10.3390/rs17111833

1. Introduction

Pine wilt disease (PWD), also known as pine tree wilt disease, is a systemic infectious disease caused by the pine wood nematode (PWN, *Bursaphelenchus xylophilus*), which is native to North America and has since spread to several countries and regions in Asia and Europe, presenting a significant ecological and economic threat to local forest ecosystems [1–3]. PWD is characterized by its wide ecological range, rapid transmission, and high mortality rates, with most trees progressing from initial infection to severe infection within 5 to 6 weeks [4,5]. Since the first discovery of PWD at Zhongshan Mountain in Nanjing, China, in 1982, it has spread to 708 county-level administrative regions across 19 provinces (autonomous regions, municipalities) as of the end of 2023. The affected area reached approximately 1.22 million hectares in 2023, resulting in the death of 7.5986 million pine trees. The disease continues to threaten China's 60 million hectares of pine forest resources, following a trend of "northward expansion and westward progression" [6,7]. Accurate monitoring of PWD-infected trees is a critical requirement for epidemic prevention and control, playing a crucial role in ensuring the sustainable development of forest ecosystems and maintaining national economic and social security.

UAV-based remote sensing technology effectively overcomes geographical limitations, offering high spatial resolution and monitoring accuracy, which makes it a widely adopted method for monitoring forest pests and diseases [8–12]. UAVs can be equipped with visible, multispectral, and hyperspectral sensors. Since visible light imagery primarily reflects color changes and has a limited number of spectral bands, it is difficult to extract spectral features from trees at different stages of disease progression. Therefore, it is mainly employed to identify trees with color changes in the late stages of the disease [13–18]. In contrast, multispectral and hyperspectral data provide richer spectral information. Compared to multispectral remote sensing data, hyperspectral imagery typically contains hundreds of bands, offering detailed narrowband information. This capability allows for the precise monitoring of subtle canopy changes and is widely applied in forest pest and disease detection [19–22]. However, current PWD control efforts primarily focus on clearing infected trees through cutting and burning after significant visual changes are observed [23]. To further safeguard the ecological integrity of pine forests and minimize economic losses, the focus of epidemic prevention and control is gradually shifting towards the early intervention of infected trees. With the development of early treatment agents, the effective identification of early stage infected trees has become a critical challenge that needs to be addressed.

Previous studies have shown a significant correlation between PWD and the moisture content and chlorophyll content of pine trees, making these parameters key physiological indicators for the early monitoring of the disease [24]. For example, Xu et al. [25] investigated changes in needle moisture content and pigment levels in pine trees naturally infected with PWD. Their results revealed a significant decrease in both needle moisture and pigment levels as the infection progressed. Li et al. [26] analyzed the moisture content of pine trees at different stages of infection in conjunction with the external symptoms of infected trees. The study revealed a positive correlation between moisture content and external symptoms throughout the entire progression of the disease. Xiang et al. [27] explored the relationship between the spectral characteristics of pine trees at different infection stages and chlorophyll content, demonstrating a significant reduction in chlorophyll content as the disease advanced. Furthermore, the physiological structure and function of pine trees undergo significant changes under the stress induced by PWD and result in distinct spectral responses [28]. Building upon these findings, researchers have investigated typical spectral features that can indicate disease stages in pine trees. Wang et al. [29] analyzed the spectral characteristic curves of *Pinus massoniana* with varying levels of damage and found that the red-green band was particularly sensitive to changes in vegetation pigments and mois-

ture. Significant differences in spectral reflectance were also observed in the near-infrared spectral region for different types of damaged trees. Huang et al. [30] integrated field measurements with airborne multispectral imagery and observed that the first derivative spectra of healthy and PWD-infected pine trees exhibited significant differences around 710 nm. Their findings suggest that the first derivative spectral regions spanning 490–530 nm and 680–760 nm are particularly effective for extracting specific hyperspectral features associated with different stages of PWD infection. In a related study, Pan Jie et al. [31] utilized a hyperspectral sensitive-band extraction method to identify key diagnostic wavelengths and subsequently constructed a false-color feature map (FCFMS) for the early detection of PWD by integrating the NDVI and RVI indices. Their findings revealed that the FCFMS could capture subtle color variations indicative of early stage infection, even before the onset of visually discernible symptoms. The spectral bands used for index synthesis were primarily concentrated in the green, red-edge, and near-infrared regions, particularly around 800 nm.

Building on the aforementioned theory, previous studies have employed UAVs equipped with hyperspectral sensors to capture detailed narrowband spectral features, which reflect subtle variations in the relative abundance and physiological activity of vegetation [32,33]. This approach facilitates the identification of early stage infected trees based on subtle changes in their canopy. For instance, Jung et al. [34] compared differences in the NDVI index of PWD-infected trees at various stages using UAV-based hyperspectral imagery. By setting an NDVI threshold, they successfully identified trees at different disease stages. The results indicated that NDVI could effectively differentiate between infected and uninfected trees and had potential for detecting early stage infections before visible color changes occurred. Huang et al. [35] developed an improved chlorophyll absorption ratio index (TCARI) based on 550 nm, 670 nm, and 700 nm wavelengths to assess its efficacy in identifying black pines at different stages of infection. The results showed that TCARI was effective for identifying late-stage trees with visible color changes, but its accuracy for early stage infected trees was relatively low. Iordache et al. [36] assessed the classification performance of information-based indices extracted from airborne multispectral and hyperspectral imagery acquired over Portugal, employing a random forest algorithm to differentiate healthy, suspected, and infected pine trees. Liu et al. [37] constructed an early infection dataset using the DW3D hyperspectral reconstruction network and achieved an early stage detection accuracy of 74% by applying a polynomial-kernel support vector machine (SVM) to spectral features across different infection stages. Zeng et al. [38] utilized UAV-based hyperspectral imagery over southern Sichuan to extract Pinus massoniana stands through band combinations and region of interest (ROI) classification, subsequently employing supervised SVM to identify early stage infected trees. Similarly, Li et al. [39] developed an integrated detection framework that combined individual-tree segmentation with a Mask R-CNN classification network, achieving an early stage infection detection accuracy of 74.89% using UAV hyperspectral data. Collectively, these studies demonstrate the effectiveness of UAV-based hyperspectral remote sensing for the early monitoring of PWD. However, most previous research has been limited to single-date UAV acquisitions and static comparative analyses for feature extraction in early stage detection. Studies employing multitemporal datasets to retrospectively identify early stage infected trees remain rare. Furthermore, prior research has primarily focused on traditional canopy pigment indices, with limited attention to canopy water content metrics for distinguishing different infection stages.

This study carried out continuous field observations in typical epidemic regions during the peak outbreak period of pine wilt disease (PWD), with the aim of identifying infected trees at various stages based on hyperspectral data and biochemical parameters. The following specific objectives were noted: (1) to improve the reliability of early stage

infected tree samples by utilizing multitemporal hyperspectral observations, and to construct a monitoring index set for PWD infection stages by selecting canopy pigment and moisture content indicators associated with key physiological processes influencing disease development; (2) to analyze the dynamic variation trends of each index within the set and identify the most effective indicators for differentiating infection stages; and (3) to develop a classification model for PWD infection stages based on the selected optimal indicators, assess its early detection performance, and investigate the relationships between early identification accuracy, infection severity, and the timing of disease onset.

2. Materials and Methods

2.1. Study Site

The experimental area is located in the Dahuofang Reservoir and Hada Forest Farms, situated in Zhangdang Town, Fushun City, in the eastern part of Liaoning Province (124°13′06″E, 41°56′15″N). The study area is characterized by a temperate continental monsoon climate, with typical features of hot, rainy summers and cold, dry winters. The average annual temperature is 6.8 °C, with an average annual precipitation of 789.5 mm. The forest farms are rich in forest resources and are predominantly composed of artificially planted species such as *Pinus koraiensis*, *Pinus tabuliformis*, and *Larix principis-rupprechtii*.

Following a year of extensive field surveys, we obtained a clear understanding of the natural dynamics of local pine stands and the patterns of occurrence and progression of PWD. Building on these insights, in the second year, we selected optimal observation periods and locations to conduct periodic field monitoring. This study was carried out in two *Pinus tabuliformis* monoculture forests affected by PWD, located near the Dahuofang Reservoir and within the Hadaling Forest Farm. Both experimental plots contained trees at varying stages of infection, thus providing suitable conditions for comparative analyses. The plot shown in Figure 1c was primarily composed of *Pinus tabuliformis* trees aged between 10 and 15 years, with heights typically ranging from 8 to 12 m and an average basal area of 359.68 cm^2. Owing to the relatively low tree density and the ease of needle sampling, this plot was mainly used for needle-level comparative analyses across different infection stages. The optimal early stage monitoring indices identified at the needle scale were subsequently extended to canopy-level evaluations. In contrast, the plot depicted in Figure 1d was predominantly composed of *Pinus tabuliformis* trees aged between 20 and 25 years, with heights generally ranging from 15 to 25 m and an average basal area of 1122.21 cm^2. Although the greater tree height posed challenges for field-based needle sampling, the higher tree density provided a more robust sample base. To further assess the applicability of the optimal early stage monitoring indices at the canopy scale, UAV-acquired hyperspectral imagery was collected over this plot. Subsequent standard pixel-based sample analysis and threshold segmentation were performed to classify infection stages and to evaluate the accuracy of early stage detection.

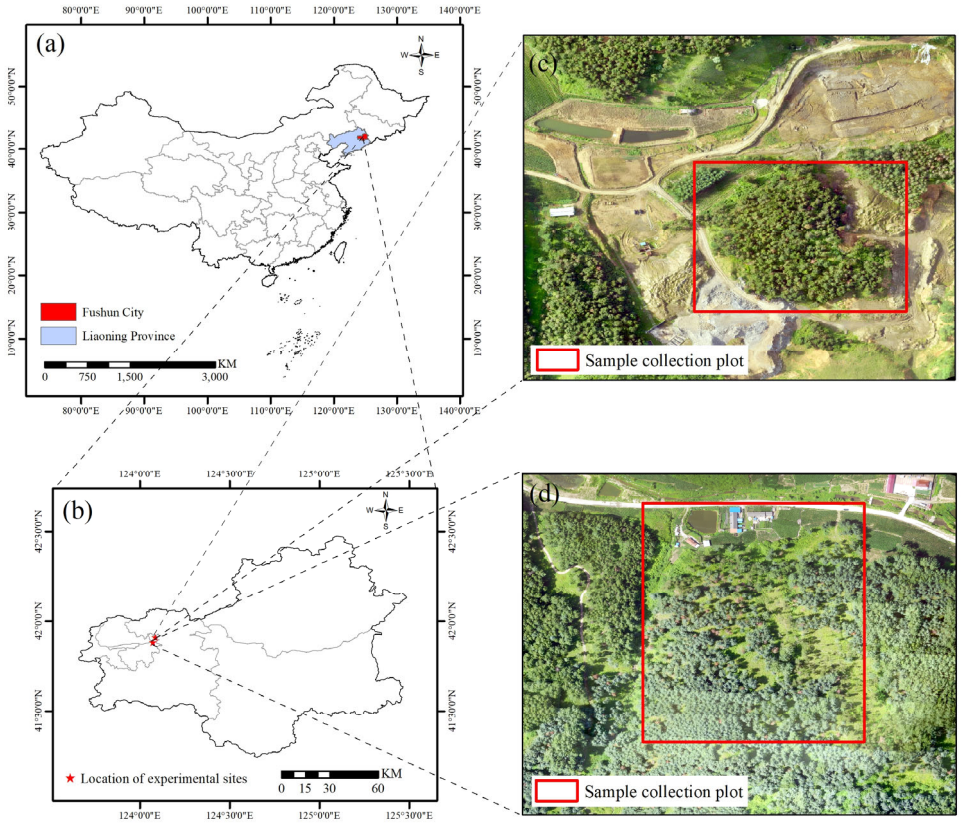

Figure 1. Study area: (**a**) the map of China; (**b**) the map of Liaoning Province; (**c**) Dahuofang Reservoir experimental area; (**d**) Hada Forest Farm experimental area.

2.2. Data Acquisition and Preprocessing

2.2.1. Ground Data Collection

From July to October 2023, continuous field observations were conducted, with on-site surveys performed once per month. Between 5 and 7 July, the following six primary tasks were completed: the selection of representative sample trees within the plots, recording of their geographic coordinates, collection of needle samples, ground-based spectral measurements using an ASD spectrometer, physiological parameter assessments, and acquisition of UAV-based hyperspectral imagery. During the subsequent three months of fieldwork, all tasks were repeated, except for the selection of representative trees and the recording of geographic coordinates. To investigate the spectral characteristics of pine needles at the leaf scale under different degrees of discoloration, the needles were categorized into the following four types based on previous research [27,39] and field observations: (1) healthy and non-discolored needles: collected from healthy trees with vigorous growth, exhibiting dark green needles; (2) slightly discolored needles: collected from trees with slowed growth and cessation of resin secretion, where the needles showed localized yellowing; (3) moderately discolored needles: collected from trees with visibly weakened growth, where the majority of the needles had turned yellow-brown and exhibited signs of wilting; (4) severely discolored (dead) needles: collected from nearly dead trees, with needles that were entirely red-brown. Based on this classification, standard branches from the sample trees were pruned and collected from the east, south, west, and north directions. The collected samples were placed in sealed bags, labeled with identification numbers, and stored in a refrigerated insulated box for preservation. The specific pine needle samples are shown in Figure 2.

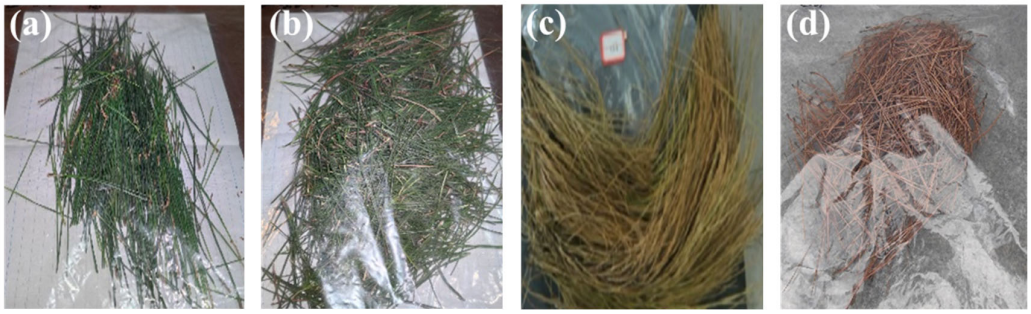

Figure 2. Images of pine needle samples at different PWD infection stages: (**a**) healthy; (**b**) mildly discolored; (**c**) moderately discolored; (**d**) severely discolored.

2.2.2. Ground ASD Spectral Data Acquisition and Processing

We employed the ASD Field Spec 4 Hi-Res NG (Analytical Spectral Devices, Boulder, CO, USA) to measure the spectra of different types of pine needle samples following the indoor spectral measurement method [40]. The spectral range spanned from 350 to 2500 nm. For each sample group (comprising a single branch of pine needles), we performed 10 repeated measurements and computed the average, which was used as the final spectral value for that group. After excluding outliers, a total of 257 valid spectral samples were obtained, including 96 healthy and non-discolored samples, 54 slightly discolored samples, 42 moderately discolored samples, and 65 severely discolored samples. The spectral curves for these four representative sample types are presented in Figure 3.

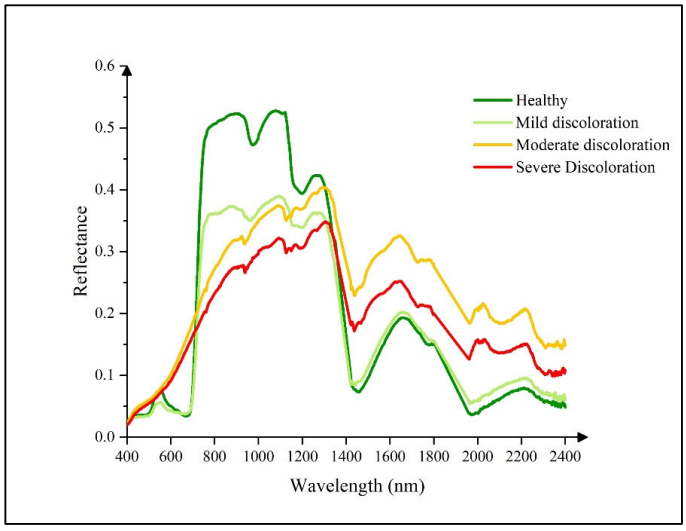

Figure 3. Average spectral reflectance of different types of pine needle samples.

2.2.3. Physiological Parameter Data Acquisition and Processing

Physiological parameters of the pine needle samples that underwent spectral measurements were determined. Chlorophyll content for each group of samples was measured using a PE Lambda 35 UV spectrophotometer [41], with five repeated readings taken and averaged to obtain the final chlorophyll content for that sample group. The moisture content of each group of pine needle samples was measured using the drying method. The statistical results of the physiological parameters for the samples are shown in Table 1 (Cab: chlorophyll content; WC: moisture content).

Table 1. Statistical results of sample physiological parameters.

	Mean	Standard Deviation	Maximum	Minimum	Coefficient of Variation
Cab (mg/g)	0.329	0.264	1.115	0.006	0.803
WC (%)	35.664	21.613	62.276	4.951	0.606

2.2.4. UAV Hyperspectral Remote Sensing Imagery Data Acquisition

A UAV system (S1000) equipped with a hyperspectral imaging sensor (X20P) (Figure 4) was used to acquire hyperspectral remote sensing imagery of the study area. The UAV hyperspectral imaging system consisted of four parts including a four-rotor electric UAV system (DJI Innovations, Shenzhen, China), a X20P hyperspectral data acquisition system (Cubert GmbH, Ulm, Baden-Württemberg, Germany), a three-axis stabilized platform, and a data processing system. The X20P sensor has a spectral range of 350–1000 nm, with a spectral resolution of approximately 4 nm [42]. In accordance with UAV monitoring technical standards and hyperspectral imaging industry specifications [43], and considering the practical research requirements for scaling from the needle level to the canopy level, UAV flight parameters were configured as follows: a flight altitude of 110 m, a flight speed of 4 m/s, a forward overlap of approximately 90%, and a side overlap of approximately 80%. At this altitude, hyperspectral imagery was acquired with a spatial resolution of 2.73 cm and a spectral resolution of 4 nm. A radiometric calibration panel was laid flat on the ground within the UAV flight area to facilitate accurate radiometric correction. Data collection was performed under clear, windless conditions to ensure optimal image quality. In this study, UAV-based hyperspectral data were collected between 11:00 a.m. and 2:00 p.m. local time.

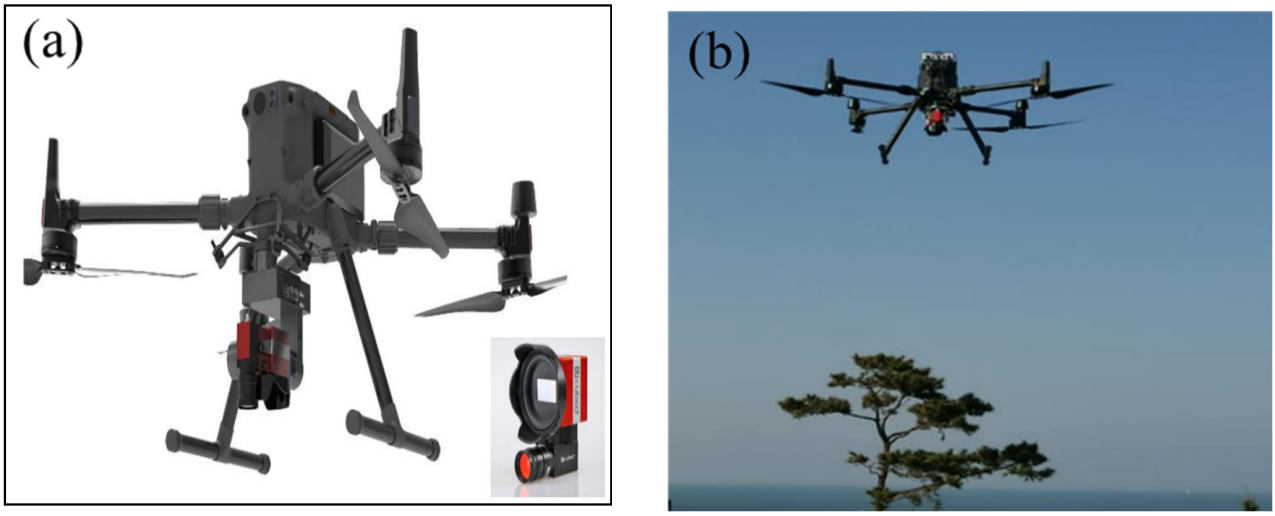

Figure 4. UAV hyperspectral imaging system and field operation conditions: (**a**) UAV hyperspectral imaging system equipped with the X20P sensor; (**b**) field operation of the UAV hyperspectral imaging system.

2.2.5. UAV Hyperspectral Remote Sensing Imagery Data Processing

The raw hyperspectral imagery obtained from the experimental plots underwent initial quality screening to remove anomalous data. Specifically, images captured during UAV takeoff, landing, and turning phases were excluded to ensure consistency and data integrity. The remaining valid images were processed using Cubert Utils software (V3.1), where pan-sharpening techniques were applied to integrate the original hyperspectral data with corresponding panchromatic images, thereby enhancing spatial resolution. Image

mosaicking and stitching were subsequently completed using Agisoft Metashape (V1.7.6). In the ensuing preprocessing workflow, radiometric correction, geometric refinement, and reflectance calibration were performed sequentially to ensure spectral accuracy and spatial alignment [44]. To minimize sensor-related noise and preserve the intrinsic spectral characteristics, the Savitzky–Golay smoothing algorithm was employed [45]. The final output comprised georeferenced airborne hyperspectral datasets in ".tiff" format, which served as the basis for canopy-scale analyses of PWD infection stages.

2.3. Methods

2.3.1. Selection of Representative Pixels from UAV Hyperspectral Imagery

To determine whether spectral characteristics of pine needles in varying infection stages—observed at the leaf scale—can be effectively extrapolated for classifying infection stages at the canopy scale, we performed feature analysis on pixel clusters within UAV-based hyperspectral imagery that approximated the spatial resolution of individual needles (Figure 5). Representative pixel samples were extracted using a standardized region of interest (ROI) tool, with each ROI consisting of 20 pixels. The mean reflectance of all pixels within each ROI was calculated to derive relevant spectral indices for further analysis. Distinct spectral signatures of pine trees at different infection stages in UAV-borne hyperspectral imagery were used to classify pixel samples into the following three categories: healthy, infected without visible discoloration, and infected with discoloration [46,47]. From each category, 50 representative pixel clusters were extracted for subsequent index analysis. To confirm that these pixel-level findings reliably and objectively represent the physiological status of trees across infection stages, we generated multiple validation datasets of equal size for comparative analysis. The criteria for pixel selection were as follows:

(1) Healthy: Based on field observations, regions of interest (ROIs) corresponding to healthy pine trees were identified in the July hyperspectral imagery. These ROIs exclusively comprised green pixels with no signs of discoloration. Furthermore, to ensure temporal consistency, only trees that exhibited no visible discoloration across all available temporal image sequences were included in this category.

(2) Infected without discoloration: ROIs in this category were retrospectively selected by integrating field survey data with multi-temporal UAV imagery. These ROIs consisted entirely of green, non-discolored pixels and met at least one of the following criteria: field observations indicated that discoloration had initiated in the lower canopy, while the upper canopy remained green or trees appeared green in the July imagery but exhibited visible discoloration (red or yellow-green tones) in later imagery (e.g., from August or October). Pixel sets were extracted from the earlier time points—prior to the onset of visible symptoms—for analysis as "infected without discoloration".

(3) Infected with discoloration: This category included ROIs representing trees with visible signs of infection as confirmed by field observations. In the July hyperspectral imagery, these ROIs were composed entirely of red or yellow-green pixels, indicative of advanced disease progression.

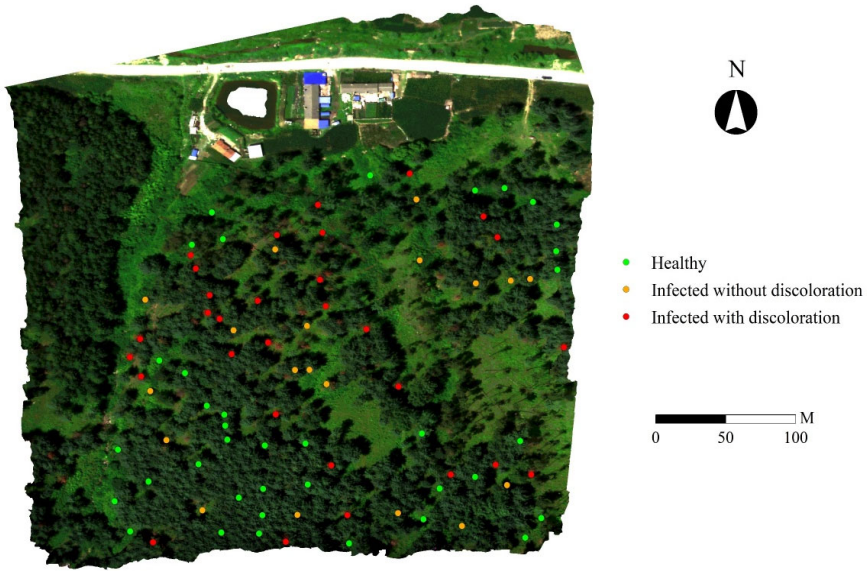

Figure 5. Examples of sample pixel selection for different categories.

2.3.2. Construction of an Indicator Set for Identifying Disease Stages in Infected Trees

Based on the pathogenic mechanism of PWD, 15 vegetation indices (including canopy pigment indices and canopy moisture content indices) were selected, which were derived from band combinations within the spectral range of 400–1000 nm from UAV hyperspectral imagery in order to construct a set of indicators for identifying infection stages of PWD. A detailed list of the selected indices is provided in Tables 2 and 3.

Table 2. Canopy pigment index set.

Variable	Description	Formula	Source
NDVI	Normalized difference vegetation index	$(R_{800} - R_{670}) / (R_{800} + R_{670})$	[34]
CI	Chlorophyll index	$(R_{850} - R_{710}) / (R_{850} + R_{680})$	[48]
PSND	Pigment-specific normalized difference	$(R_{800} - R_{680}) / (R_{800} + R_{680})$	[27]
PSSR	Pigment specific simple ratio	R_{800} / R_{680}	[49]
RVSI	Ratio vegetation stress index	R_{600} / R_{760}	[50]
PSI	Plant stress index	R_{695} / R_{760}	[38]
TCARI	Transformed chlorophyll absorption Ratio index	$3[(R_{700} - R_{670}) - 0.2(R_{700} - R_{550}) / (R_{700} / R_{670}))$	[35]
ARI	Anthocyanin reflectance index	$(R_{550})^{-1} - (R_{700})^{-1}$	[51]
GI	Greenness index	R_{554} / R_{677}	[52]
SIPI	Structural independent pigment index	$(R_{800} - R_{445}) / (R_{800} + R_{680})$	[53]

Table 3. Canopy moisture content index set.

Variable	Description	Formula	Source
WI1	Water index 1	R_{970}/R_{900}	[54]
WI2	Water index 2	R_{950}/R_{900}	[55]
WASCOSBNDI	Water absorption shoulder due to combined overtone of stretching bands—normalized difference index	$(R_{800} - R_{847})/(R_{800} + R_{847})$	[56]
COSBNDI	Combined overtone of stretching bands—normalized difference index	$(R_{660} - R_{420})/(R_{660} + R_{420})$	[57]
SAPSBNDI	Small absorption peak of stretching bands—normalized difference index	$(R_{750} - R_{970})/(R_{750} + R_{970})$	[57]

Correlation analysis was conducted to select the three canopy pigment and canopy moisture content indices with the highest correlation coefficients to the field-collected pigment and moisture content samples for the subsequent comparison analysis of the optimal indicators. The formula for calculating the correlation coefficient (R) is [58] as follows:

$$\mathrm{R} = \frac{\sum_{i=1}^{n}(Y_i - \overline{Y_i})(Y_i' - \overline{Y_i'})}{\sqrt{\sum_{i=1}^{n}(Y_i - \overline{Y_i})^2}\sqrt{\sum_{i=1}^{n}(Y_i' - \overline{Y_i'})^2}} \quad (1)$$

2.3.3. Optimal Indicator Analysis and Disease Stage Monitoring Model Construction

The candidate indicators obtained in the previous section were subjected to optimal selection to further improve the efficiency of infected tree identification. Significance tests were conducted to determine whether there were significant differences in the indicator values between different disease stages. Derivative analysis was then performed to calculate the rate of change (k) [59] of the indicators between stages. The absolute value of k was taken as the magnitude of change (m), with the specific calculation formula as follows:

$$\mathrm{k} = \frac{\overline{x_{n+1}} - \overline{x_n}}{\overline{x_n}} \times 100\% \quad (2)$$

$$\mathrm{m} = |\mathrm{k}| \quad (3)$$

where $\overline{x_n}$ represents the average value of the indicator for the sample at stage n, and $\overline{x_{n+1}}$ represents the average value of the indicator for the sample at the next stage.

Based on previous studies on the physiological changes in pine trees during the development of pine wilt disease [24–27], the vegetation index with significant differences and the largest rate of change between the healthy and infected non-discolored stages was selected as the optimal canopy moisture content index. The vegetation index with the largest average rate of change between the healthy–infected non-discolored stage and the infected non-discolored–infected discolored stage was selected as the optimal canopy pigment index. These optimal indices for canopy pigment and moisture content were then used to construct the disease stage identification model for pine trees.

In this paper, we constructed the disease stage identification model for pine trees based on the threshold segmentation method [60]. The model's performance was evaluated using significance testing and accuracy assessments. Model development consisted of the following two principal steps: (1) establishing the optimal classification thresholds and (2) converting the raw classification outputs into definitive infection-stage labels. The detailed workflow is as follows:

(1) The optimal classification threshold was determined for each individual indicator. A scatter plot of the indicators in a two-dimensional plane was generated to analyze the distribution pattern of the samples. The one-dimensional feature threshold segmentation method was employed to search for the classification threshold α within the indicator range corresponding to the two categories. The step size for searching α was adaptively adjusted according to the indicator accuracy. The goal was to minimize the intra-group distance and maximize the inter-group distance. The discrimination index J_f was then constructed, as follows [61]:

$$J_f = \frac{(m_1 - m_2)^2}{S_1^2 + S_2^2} \tag{4}$$

The classification threshold α corresponding to the maximum value of J_f was selected as the optimal threshold. In the formula, m_1 and m_2 represent the means of the two sample classes, while S_1^2 and S_2^2 represent the variances of the two sample classes. The calculation formulas for the mean (m) and variance $\left(S^2\right)$ are as follows [62]:

$$m = \frac{\sum_{i=1}^{n} x_i}{n} \tag{5}$$

$$S^2 = \frac{\sum_{i=1}^{n} (x_i - \overline{x})}{n} \tag{6}$$

where x_i represents the individual sample value, $\overline{x}$ represents the sample mean, and n is the sample size.

(2) The optimal decision boundary was obtained based on combined indicators. A scatter plot of the indicators and the 95% confidence ellipses for each class of samples were plotted in the two-dimensional plane. The sample distribution was analyzed, and Linear Discriminant Analysis (LDA) was applied to reduce dimensionality and to classify the data [63]. To maximize the differences between different classes of samples, the discriminant index J (generalized Rayleigh quotient) was calculated, as follows [62]:

$$J = \frac{\omega^T S_b \omega}{\omega^T S_\omega \omega} \tag{7}$$

In Equation (7), ω represents the projection vector, ω^T is the transpose of the projection vector, S_b is the between-class scatter matrix, and S_ω is the within-class scatter matrix. The calculation formulas for S_b and S_ω are as follows [64]:

$$S_b = (\mu_0 - \mu_1)(\mu_0 - \mu_1)^T \tag{8}$$

$$S_\omega = \sum_{x \in X_0} (x - \mu_0)(x - \mu_0)^T + \sum_{x \in X_1} (x - \mu_1)(x - \mu_1)^T \tag{9}$$

In Equations (8) and (9), μ_i represents the mean vector of the i-th class, and X_i represents the sample set corresponding to the i-th class.

(3) The single-indicator and composite-indicator approaches were applied to classify pine trees at different infection stages. Using the optimally validated segmentation thresholds derived previously, each pixel in the UAV hyperspectral imagery was assigned an infection-stage label. To improve classification reliability, the following spatial consistency check was then applied: if all neighboring pixels around a target pixel were assigned a different class than the target, then the target pixel was flagged as anomalous and its label reassigned to the majority class of its neighbors; otherwise, the original classification was retained.

As the threshold-based segmentation generated results at the pixel level, an additional step was required to upscale these to object-level classifications—specifically, to assign infection stages at the individual tree level. This conversion is crucial for real-world applications, such as the targeted monitoring of pine wilt disease-infected trees. By drawing on field observations and pixel-level classifications, and acknowledging the inherent spectral heterogeneity within individual tree crowns, we established the following object-level classification criteria, based on prior research [65,66]: (1) if a tree crown exhibited obvious discoloration, then it was classified as "infected with discoloration"; (2) if no visible discoloration was present, but more than 30% of the pixels within the crown were classified as "infected without discoloration", then the tree was labeled accordingly; (3) all remaining trees were classified as healthy.

2.3.4. Accuracy Evaluation

We employed standardized accuracy assessment methods to evaluate the performance of the disease stage identification model for infected trees. Using a general binary classification accuracy evaluation approach, we calculated three basic metrics for the detection results based on different models: True Positive (TP), False Positive (FP), and False Negative (FN). Specifically, TP represents instances where the model's detection of pine trees aligns with field survey results, FP refers to instances where the model's detection does not match the field survey results, and FN represents cases where the field survey results were not correctly identified by the model. After obtaining the relevant statistical results, we assessed the model's ability to identify disease stages in infected trees using three commonly applied accuracy metrics, which were Producer's Accuracy (Recall), User's Accuracy (Precision), and Overall Accuracy (F1 score), calculated using the following formulas [67]:

$$\text{Precision} = \frac{\text{TP}}{\text{TP} + \text{FP}} \tag{10}$$

$$\text{Recall} = \frac{\text{TP}}{\text{TP} + \text{FN}} \tag{11}$$

$$\text{F1 score} = \frac{2 \times \text{P} \times \text{R}}{\text{P} + \text{R}} \tag{12}$$

where User's Accuracy reflects the proportion of correctly detected instances within the identified category, Producer's Accuracy measures the proportion of correctly detected instances for a particular tree category in the field, and the F1 score represents the overall effectiveness of the model in distinguishing between different disease stages in infected trees. A higher F1 score indicates better differentiation of disease stages by the model.

3. Results

3.1. Construction of Disease Stage Identification Indicator Set and Selection of Optimal Indicators

Based on the physiological measurements obtained from field-sampled pine needles, correlation analyses were performed to assess the effectiveness of conventional spectral indices in representing canopy-level pigment concentration and water content (Figure 6).

For each physiological trait, the three indices exhibiting the highest correlation coefficients were selected. These were subsequently used to construct two canopy-scale diagnostic index sets, which were a pigment-related index set (CI, NDVI, and PSND) and a water-content-related index set (WASCOSBNDI, SAPSBNDI, and WI2).

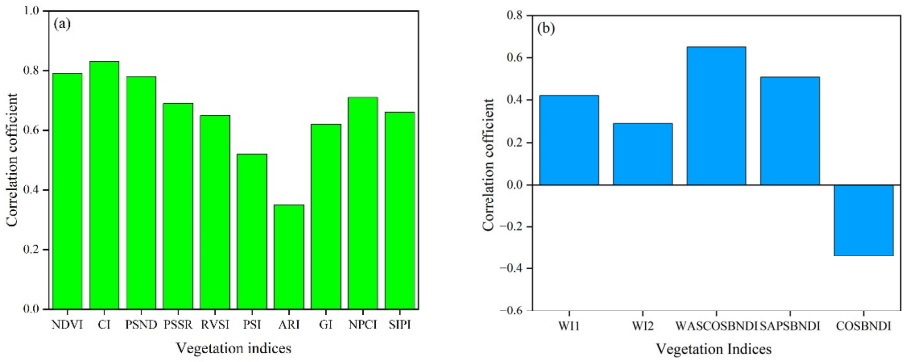

Figure 6. The correlation between the field-measured physiological parameters of the samples and different features: (**a**) pigment index and field-measured pigment content of the samples; (**b**) moisture content index and field-measured moisture content of the samples.

The results showed that, within the canopy moisture content indicator set, WASCOSBNDI exhibited a significant difference between the healthy and non-discolored infected stages ($p < 0.01$), with an average rate of change of 0.045 (Table 4). In the late stages of infection, all three indicators displayed significant differences between the two stages ($p < 0.01$), although the overall difference in the average rate of change was relatively small. This suggests that moisture content indicators are generally more sensitive to moisture changes in infected trees during the late stages of disease. Considering these findings, WASCOSBNDI, which showed the highest average rate of change between the healthy and non-discolored infected stages, was selected for subsequent model construction. In the canopy pigment indicator set, no significant differences were found for any of the indices in the early infection stages ($p > 0.05$), with average rates of change generally remaining in the range of [−5%, 0] (Table 5). However, significant differences were observed in the mid-to-late infection stages, with the average rates of change being considerably higher than in the early stages. Among the indices, CI exhibited the largest variation in the healthy and non-discolored infected stages. Given that the average rate of change between the two stages for the three indices was relatively similar, CI was selected for subsequent model construction (Figure 7).

Table 4. Rate of change in canopy moisture content indices.

Moisture Content Index	Healthy—Infected but Non-Discolored	Infected but Non-Discolored—Infected and Discolored
WASCOSBNDI	−133.73% **	459.02% **
SAPSBNDI	−15.57%	362.49% **
WI1	−12.17%	184.76%**

Note: ** indicates that the correlation was significant at the 0.01 level.

Table 5. Rate of change in canopy pigment indices.

Pigment Index	Healthy—Infected but Non-Discolored	Infected but Non-Discolored—Infected and Discolored
CI	−4.97%	−43.22% **
NDVI	−1.52%	−45.84% **
PSND	−1.66%	−44.37% **

Note: ** indicates that the correlation was significant at the 0.01 level.

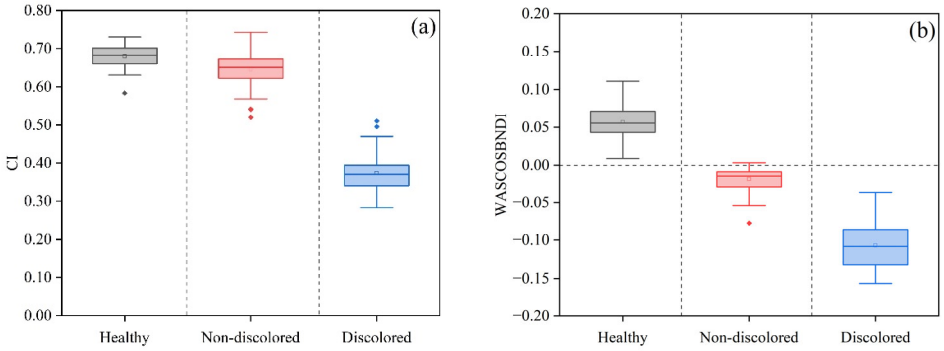

Figure 7. Variation of standard indicator characteristics at different stages: (**a**) CI Index; (**b**) WASCOSBNDI Index.

3.2. Construction of PWD Stage Identification Model for Infected Trees

Threshold analysis was conducted on representative pixel-level index values extracted from UAV hyperspectral imagery, and the resulting segmentation thresholds were rigorously validated through multiple iterations using independent validation datasets. Figure 8 presents the optimal segmentation maps derived via linear discriminant analysis, and Table 6 lists the optimal thresholds—both for individual indices and their composites—employed to distinguish among the various sample classes. Based on the distribution of the three sample categories in the two-dimensional feature space, it can be observed that the samples from different infection stages exhibit a relatively well-defined linear separability. The discrimination formulas for the dual-indicator analysis of individual pixels are as follows: (1) when 0.126CI + WASCOSBNDI—0.101 $\geq$ 0, the pixel is classified as healthy; (2) when 0.126CI + WASCOSBNDI—0.101 < 0 and 1.103CI + WASCOSBNDI—0.522 $\geq$ 0, the pixel is classified as infected but non-discolored; (3) when 1.103CI + WASCOSBNDI—0.522 < 0, the pixel is classified as infected and discolored. The results indicate that classification based solely on the CI index causes significant misclassification between the infected non-discolored and healthy categories. When classification was based solely on WASCOSBNDI, a small number of misclassifications occurred between the non-discolored infected category and the other two categories. However, when using the combined dual indicators, the overlap between the three disease stages was further reduced, allowing for a clearer distinction of the disease stage of pixel samples. Building upon this, we developed models for identifying the infection stages of PWD based on the pigment index CI, moisture content index WASCOSBNDI, and the combined index CI-WASCOSBNDI, and we applied these models to detect the infection stages of pine trees within the study area. Subsequently, we conducted a further investigation to assess the practical application of these indices for the early detection of infected trees.

Table 6. Classification thresholds for different indicators.

	CI	WASCOSBNDI	CI-WASCOSBDI
Healthy—Infected but Non-Discolored	0.52	0.015	0.126CI + WASCOSBNDI – 0.101 = 0
Infected but Non-Discolored—Infected and Discolored	0.67	−0.048	1.103CI + WASCOSBNDI – 0.522 = 0

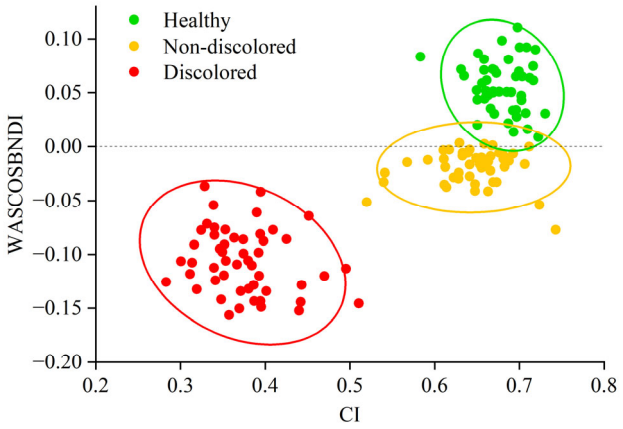

Figure 8. Multiple threshold segmentation results.

3.3. Early Detection and Accuracy Evaluation of PWD Infected Trees

After model construction, the segmentation of individual trees was performed using the object-oriented classification function in ENVI 5.3 software. After removing irrelevant background information, the boundaries of the extracted individual tree objects were manually corrected, forming the final object set for the identification of disease stages in pine trees. Canopy-level tree status classification was ultimately derived from the pixel-level identification results, following the previously established scale conversion criteria.

Figure 9 and Tables 7–9 present the recognition results and accuracy of PWD stages based on different classification models. The CI model achieved an overall accuracy of 81.82% in classifying pine tree disease stages, with excellent performance in identifying trees at the infected and discolored stage, where the recognition accuracy exceeded 90%. However, it struggled to accurately identify infected but non-discolored trees at the early stage of PWD, with a recognition accuracy of only 25%. In contrast, based on the WASCOSBNDI model, the overall accuracy for classifying the disease stages of pine trees reached 89.31%, showing a significant improvement compared to the CI model. The WASCOSBNDI model had a recognition accuracy of 66.7% for infected but non-discolored trees, which was notably better than the CI model. However, its recognition accuracy for discolored infected trees was slightly lower than that of the CI model. The CI-WASCOSBNDI model, combining both indicators, achieved an overall accuracy of 92.78%, which was significantly higher than both the CI and WASCOSBNDI models. This model accurately monitored healthy pine trees and infected trees at the discolored stage with recognition accuracies of 94.9% and 95.45%, respectively. For infected but non-discolored trees, the recognition accuracy was 72.22%, representing a 6.05% improvement over the WASCOSBNDI model.

Table 7. Accuracy validation based on CI model recognition.

Stage	Healthy	Infected but Non-Discolored	Infected and Discolored	Total	PA (%)
Healthy	246	48	0	294	83.67%
Infected but Non-Discolored	27	9	0	36	25%
Infected and Discolored	0	2	42	44	95.45%
Total	273	59	42	374	
UA (%)	90.11%	15.25%	100%	OA (%)	81.82%

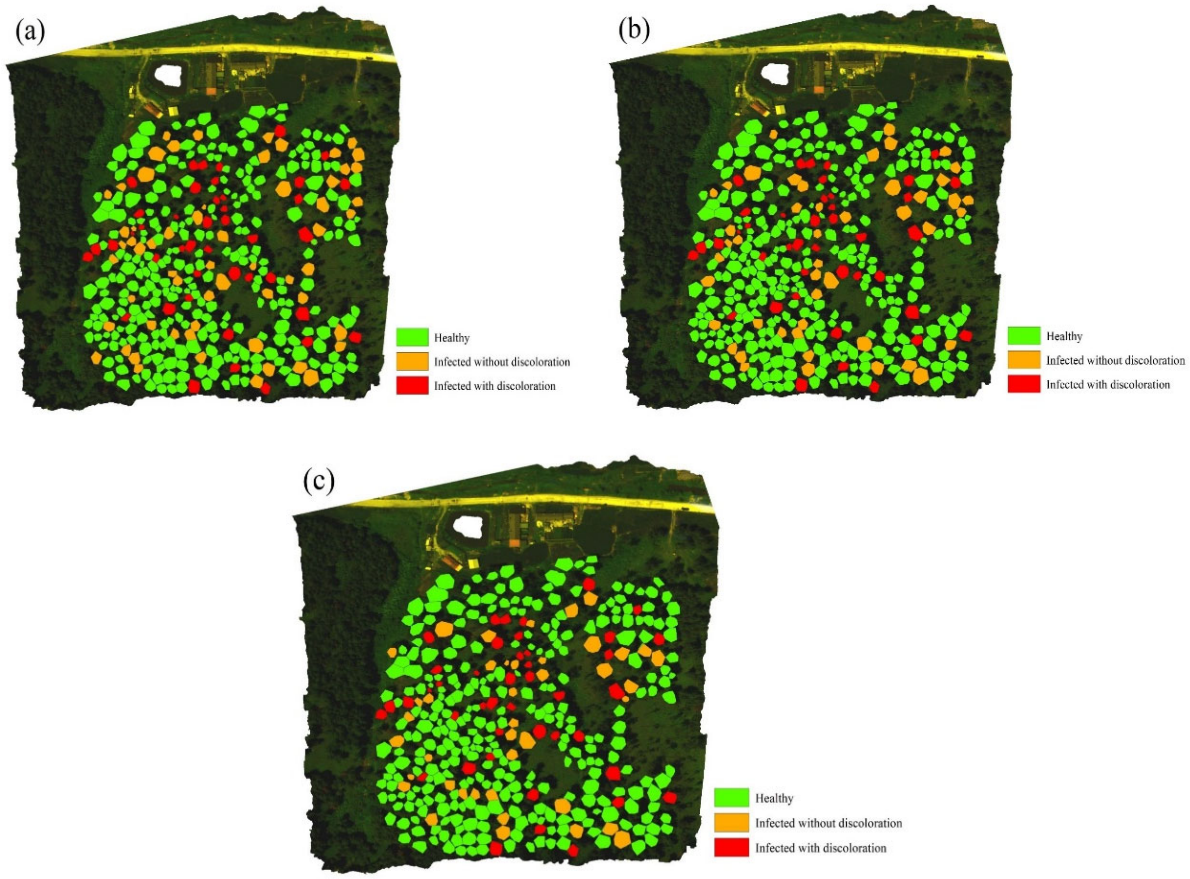

Figure 9. Recognition results of the infected stage of diseased trees based on different models: (**a**) CI model; (**b**) WASCOSBNDI model; (**c**) CI-WASCOSBNDI model.

Table 8. Accuracy validation based on WASCOSBNDI model recognition.

Stage	Healthy	Infected but Non-Discolored	Infected and Discolored	Total	PA (%)
Healthy	271	23	0	294	92.18%
Infected but Non-Discolored	11	24	1	36	66.67%
Infected and Discolored	0	5	39	44	88.64%
Total	282	52	40	374	
UA (%)	96.1%	46.15%	97.5%	OA (%)	89.31%

Furthermore, we explored the relationship between the CI-WASCOSBNDI model and the disease severity as well as the onset time of infected trees. By combining field surveys and multi-temporal image comparisons, we found that infected but non-discolored trees in the study area were divided into the following two categories: those that became discolored by August and those that became discolored by October. Table 10 shows the recognition results of early stage infected trees based on the CI-WASCOSBNDI model. The results indicate that the model performed well in identifying trees that became discolored by August, with a recognition accuracy of 83.3%. However, it struggled to identify trees that became discolored by October, with a recognition accuracy of only 16.7%.

Table 9. Accuracy validation based on CI-WASCOSBNDI model recognition.

Stage	Healthy	Infected but Non-Discolored	Infected and Discolored	Total	PA (%)
Healthy	279	15	0	294	94.9%
Infected but Non-Discolored	10	26	0	36	72.22%
Infected and Discolored	0	2	42	44	95.45%
Total	289	43	42	374	
UA (%)	96.54%	60.47%	100%	OA (%)	92.78%

Table 10. Comparison of recognition accuracy for infected but non-discolored trees based on the CI-WASCOSBNDI collaborative index.

Stage	Healthy	Infected but Non-Discolored	Infected and Discolored	PA (%)
Discoloration by August	5	25	0	83.3%
Discoloration by October	5	1	0	16.7%

4. Discussion

4.1. Optimal Indicator Selection for Early Recognition of Infected Trees

The pigment indicators of the pine canopy exhibit significant changes during the transition from susceptible but unchanged to susceptible with discoloration, but they show minimal variation in the early stages of disease. This is consistent with previous studies describing the external characteristics of early stage infected trees [36,68]. The CI index shows the highest rate of change during the early stage of infection, likely due to its combination of spectral bands that are sensitive to both pigments and water content. In contrast, other pigment indices are primarily based on two-band difference normalization methods, which contain less spectral information and thus exhibit a lower rate of change during the early stage of infection compared to the CI index. On the other hand, the water content indicators in the pine canopy show significant changes during the transition from healthy to susceptible but unchanged and from susceptible but unchanged to susceptible with discoloration, which also corresponds to findings from previous studies on moisture changes in pine trees infected by PWD [26,27]. Among these, the WASCOSBNDI index shows the highest rate of change during the early development stage from healthy to susceptible but unchanged. This may be due to the combination of spectral bands used in the WASCOSBNDI index [56], which is more sensitive to slight changes in water content compared to other water absorption peaks. However, due to limitations imposed by the objective geographic environment, the total sample size selected in this study was limited, and only specific pine tree species were investigated. Therefore, the generalizability of the selected indicators for early stage disease recognition in pine trees requires further exploration.

4.2. Analysis of Collaborative Recognition Effect Based on Canopy Pigment-Water Content Indicators

In this study, we developed a CI monitoring model, WASCOSBNDI monitoring model, and CI-WASCOSBNDI monitoring model to identify PWD trees at different infection stages.

The results demonstrated that the CI-WASCOSBNDI monitoring model achieved the best identification performance, with an overall accuracy of 92.78%. Further comparison revealed that the moisture content index contributed the most to identifying early stage infected trees. The accuracy of identifying early stage infected trees using the WASCOSBNDI index alone was 66.7%, while the accuracy using the CI index alone was only 25%. This discrepancy may arise because the water content index primarily reflects internal physiological changes and cellular structure alterations within the leaf, while pigment indices focus on external leaf color and shape [4,24,25,33,69]. In the early stages of disease, infected trees do not exhibit significant visual differences from healthy trees, but internal tracheal cells have formed cavities that obstruct water transport, leading to a significant reduction in transpiration [2,5,26]. Therefore, changes in internal water content are more sensitive in the early stages of infection than external visual characteristics. Monitoring dynamic changes in canopy water content can thus help detect early signs of infection and significantly improve the accuracy of early recognition. In contrast, during the late stages of infection, the conductive tissues inside the tree have been severely damaged, causing a drastic decline in water content, while the external color changes from green to yellow-brown or reddish-brown. As a result, both canopy pigment and water content indicators can achieve high accuracy in identifying late-stage infected trees. However, the recognition of trees at this stage is more convenient and efficient using canopy pigment indicators.

4.3. Analysis of Early Recognition Model and Its Relationship with Disease Severity and Onset Time

Building upon the optimal early detection model, we also explored its relationship with infection severity and onset time. After comparing the images of the Hada Forest Farm from July, August, and October, we found that 30 trees with uncolored infection in July exhibited discoloration in August, while six trees showed discoloration only by October. The recognition accuracy for trees that were discolored in August was 83.34%, but for those that discolored in October, the accuracy was only 16.67%. This indicates that the model performs better in recognizing early stage infected trees that show significant discoloration near the onset of the disease but struggles to identify those that are still in the early stages of infection with more subtle changes. The reason for this may be that, in the early stages of PWD infection, the physiological changes within the pine trees are too subtle compared to healthy trees, making it difficult to extract reliable information on infected trees through remote sensing spectral analysis. However, as the infection progresses and trees approach the disease onset, even though external features may still be indistinguishable, the canopy water content significantly decreases due to continued infection, producing specific spectral responses that can be captured in sensitive spectral indices. Thus, spectral weak information enhancement can improve the monitoring accuracy for early stage infected trees [32,70,71]. It is also important to note that the critical time for effectively identifying discolored diseased trees in this study is specific to the geographical environment of the Masson pine. The relationship between the recognition model and the discolored diseased trees from different species or regions, as well as the corresponding disease onset times, may be more complex and warrants further comparative analysis through multi-region field observations in the future. Due to practical constraints associated with instrumentation and field sampling conditions, the data acquisition frequency in this study was limited to once per month. This relatively coarse temporal resolution may have led to the omission of transient symptom dynamics—such as brief discoloration events followed by rapid recovery—thereby limiting the accuracy in pinpointing critical windows during the early progression of infection. To address this limitation, future studies will incorporate dynamic, high-frequency monitoring protocols, with sampling intervals shortened to weekly or even

every three days. Such improvements are expected to enhance the detection of early stage symptom expression and enable the more precise identification of sensitive periods in the development of PWD.

5. Conclusions

This study utilized UAV hyperspectral remote sensing imagery to monitor and identify trees at different stages of PWD. Based on the findings, the following conclusions can be drawn: (1) The CI monitoring model provides the highest recognition accuracy for trees with discoloration, but it is ineffective in identifying trees in the early stages of disease. The WASCOSBNDI monitoring model can accurately identify trees in the infected but non-discolored stage, but its recognition accuracy for diseased trees with discoloration at the infected stage was slightly lower than the CI monitoring model. (2) The CI-WASCOSBNDI monitoring model achieves the highest overall recognition accuracy, including the highest accuracy for identifying infected but non-discolored trees, with an accuracy exceeding 70%. It is suitable for the early detection of PWD. (3) The CI-WASCOSBNDI monitoring model shows exceptional recognition performance for trees approaching the disease outbreak stage (approximately one month before discoloration symptoms appear), with an accuracy of 83.3%. However, it struggles to identify trees that have just been infected with the PWD (approximately three months before discoloration symptoms), with an accuracy of only 16.7%. Future studies will focus on improving the precise monitoring of PWD early stage infections to provide scientific evidence and theoretical support for timely disease prevention and control.

Author Contributions: Conceptualization, R.H.; methodology, R.H., B.Z. and W.H.; validation, R.H.; formal analysis, R.H.; investigation, R.H. and B.Z.; data curation, R.H., G.F., H.S., J.Y. (Jiayu Yan), S.Y. and L.G.; writing—original draft preparation, R.H.; writing—review and editing, R.H., B.Z., W.H., S.Y. and L.G.; supervision, B.Z., Q.J., J.Y. (Jing Yao) and W.H.; funding acquisition, W.H. All authors have read and agreed to the published version of the manuscript.

Funding: This research was funded by National Natural Science Foundation of China (42201355), Sino-UK Crop Pest and Disease Forecasting and Management Joint Laboratory, SINO-EU Dragon 6 proposal (ID 95250), GEO-PDRS: Global Vegetation Pest and Disease Dynamic Remote Sensing Monitoring and Forecasting.

Data Availability Statement: The original contributions presented in this study are included in the article. Further inquiries can be directed to the corresponding author.

Acknowledgments: The authors sincerely thank the leadership, staff, and members of the Forest Pest and Disease Remote Sensing Monitoring Group at the Biological Disaster Prevention and Control Center of the National Forestry and Grassland Administration for their generous support and assistance during the field experiments. In addition, the authors express their heartfelt gratitude to Wenjiang Huang and Biyiao Zhang for their invaluable guidance on the experimental design, manuscript preparation, and formatting of this study. We also appreciate the beneficial and constructive comments provided by the reviewers, which have significantly improved the manuscript.

Conflicts of Interest: The authors declare no conflicts of interest.

References

1. Vicente, C.; Espada, M.; Vieira, P.; Mota, M. Erratum to: Pine wilt disease: A threat to European forestry. *Eur. J. Plant Pathol.* **2012**, *133*, 497. [CrossRef]
2. Douda, O.; Zouhar, M.; Maňasová, M.; Dlouhý, M.; Lišková, J.; Ryšánek, P. Hydrogen cyanide for treating wood against pine wood nematode (*Bursaphelenchus xylophilus*): Results of a model study. *J. Wood Sci.* **2015**, *61*, 204–210. [CrossRef]
3. Tao, H.; Li, C.; Zhao, D.; Deng, S.; Hu, H.; Xu, X.; Jing, W. Deep learning-based dead pine trees detection from unmanned aerial vehicle images. *Int. J. Remote Sens.* **2020**, *41*, 8238–8255. [CrossRef]

4. Syifa, M.; Park, S.-J.; Lee, C.-W. Detection of the pine wilt disease tree candidates for drone remote sensing using artificial intelligence techniques. *Engineering* **2020**, *6*, 919–926. [CrossRef]
5. Liu, W.; Chang, Q.; Guo, M.; Xing, D.; Yuan, Y. Monitoring of leaf nitrogen content in summer corn with first derivative of spectrum based on modified red edge. *J. Northwest A F Univ.* **2010**, *38*, 91–98. [CrossRef]
6. Pan, L.; Li, Y.; Liu, Z.; Meng, F.; Chen, J.; Zhang, X. Isolation and identification of pine wood nematode in *Pinus koraiensis* in Fengcheng, Liaoning Province. *Forest Pest Dis.* **2019**, *38*, 1–4. [CrossRef]
7. Hyun, M.W.; Kim, J.H.; Suh, D.Y.; Lee, S.K.; Kim, S.H. Fungi isolated from pine wood nematode, its vector Japanese pine sawyer, and the nematode-infected Japanese black pine wood in Korea. *Mycobiology* **2007**, *35*, 159–161. [CrossRef]
8. Firtha, F. Development of data reduction function for hyperspectral imaging. *Prog. Agric. Eng. Sci.* **2007**, *3*, 67–88. [CrossRef]
9. Näsi, R.; Honkavaara, E.; Lyytikäinen-Saarenmaa, P.; Blomqvist, M.; Litkey, P.; Hakala, T.; Viljanen, N.; Kantola, T.; Tanhuanpää, T.; Holopainen, M. Using UAV-based photogrammetry and hyperspectral imaging for mapping bark beetle damage at tree-level. *Remote Sens.* **2015**, *7*, 15467–15493. [CrossRef]
10. Du, H.; Ge, H.; Fan, Y.; Jin, W.; Li, J. Application of fractal theory in hyperspectral detecting the early stage of pine wood nematode disease (*Bursaphelenchus xylophilus*) of *Pinus massoniana* with hyperspectrum. *Sci. Silv. Sin.* **2009**, *45*, 68–76. [CrossRef]
11. Shen, P.; Shao, Y. UAV + hyperspectral brings new opportunities for forest pest and disease remote sensing monitoring. *Chin. J. Geod. Geodyn.* **2022**, *2022*, 76–77.
12. Zhao, H.; Shu, Q.; Wang, K.; Yuan, Z.; Tan, D. Application of Hyperspectral Remote Sensing Technology in Forest Pest and Disease Monitoring. *Green Sci. Technol.* **2020**, *19*, 145–148. [CrossRef]
13. Huang, H.; Ma, X.; Hu, L.; Huang, Y.; Huan, H. Preliminary application of Fast R-CNN deep learning combined with UAV remote sensing in the monitoring of pine wilt disease. *J. Environ. Entomol.* **2021**, *43*, 1295–1303.
14. Li, F.; Shen, W.; Wu, J.; Sun, F.; Xu, L.; Liu, Z.; Lan, P. Research on pine wilt disease tree detection based on YOLOv3-CIoU. *J. Shandong Agric. Univ. (Nat. Sci. Ed.)* **2021**, *52*, 224–233.
15. Wang, C.; Zhang, H.; Le, J.; Zhao, S. Pine wilt disease detection using deep learning and remote sensing imagery. *J. Nanjing Norm. Univ. (Nat. Sci. Ed.)* **2021**, *44*, 84–89.
16. Zhang, P.; Wang, Z.; Rao, Y.; Zheng, J.; Zhang, N.; Wang, D.; Zhu, J.; Fang, Y.; Gao, X. Identification of pine wilt disease infected wood using UAV RGB imagery and improved YOLOv5 models integrated with attention mechanisms. *Forests* **2023**, *14*, 588. [CrossRef]
17. Jie, Y.; Ruirui, Z.; Joonwhoan, L. A deep learning-based generalized system for detecting pine wilt disease using RGB-based UAV images. *Remote Sens.* **2021**, *14*, 150. [CrossRef]
18. Han, Z.; Hu, W.; Peng, S.; Lin, H.; Zhang, J.; Zhou, J.; Wang, P.; Dian, Y. Detection of standing dead trees after pine wilt disease outbreak with airborne remote sensing imagery by multi-scale spatial attention deep learning and Gaussian kernel approach. *Remote Sens.* **2022**, *14*, 3075. [CrossRef]
19. Choi, I.W.; Park, Y. Monitoring, assessment, and management of forest insect pests and diseases. *Forests* **2019**, *10*, 865. [CrossRef]
20. Duarte, A.; Borralho, N.; Cabral, P.; Caetano, M. Recent advances in forest insect pests and diseases monitoring using UAV-based data: A systematic review. *Forests* **2022**, *13*, 911. [CrossRef]
21. Bai, X.; Zhang, X.; Zhang, N.; Ma, Y. Hyperspectral remote sensing monitoring model for the degree of damage by the pine caterpillar. *J. Beijing For. Univ.* **2016**, *38*, 16–22. [CrossRef]
22. Chen, P.; Xie, Y.; Liu, S.; Zhang, L. Exploration of Real-Time Monitoring Technology for Forest Pests and Diseases Using UAV Remote Sensing. *Sci. Technol. Innov.* **2020**, *34*, 60–61.
23. Dong, Y.; Yan, H.; Pan, J.; Zhang, Y.; Guan, Z.; Yan, J. Control strategies for pine wood nematode disease in China. *Chin. J. For. Pest Dis.* **2022**, *41*, 1–8. [CrossRef]
24. Hu, L.; Wu, X. Research progress on the mechanisms of pine tree resistance to pine wood nematode disease. *Life Sci.* **2018**, *30*, 659–666. [CrossRef]
25. Xu, H.; Luo, Y.; Zhang, Q. Changes in water content, pigments, and antioxidant enzyme activities in pine needles of *Pinus thunbergii* and *Pinus massoniana* affected by pine wood nematode. *Sci. Silvae Sin.* **2012**, *11*, 140–143.
26. Li, X.; Huang, H.; Huang, Y.; Fan, J.; Wu, H.; Wu, J. Study on the changes in disease process characteristics of pine wood nematode. *Guangdong For. Sci. Technol.* **2010**, *26*, 92–96.
27. Xiang, R.; Yuan, L.; Qin, L.; Song, Q.; Zhang, J.; Qu, Y.; Zhou, J. Correlation analysis between spectral characteristic parameters and chlorophyll content of pine needles. *Sci. Technol. Innov.* **2018**, *35*, 5–7.
28. Hu, H. UAV Remote Sensing Monitoring Technology: Building a New Line of Defense for Pest and Disease Control with Intelligent Technology—Taking the Application of UAV Remote Sensing Monitoring Technology in the Detection and Survey of Pine Wilt Disease as an Example. *China For. Ind.* **2023**, *6*, 24–25.
29. Wang, Z.; Zhang, X.; An, S. Spectral characteristics of pine trees in *Pinus massoniana* forests affected by pine wood nematode disease. *Remote Sens. Technol. Appl.* **2007**, *3*, 367–370.

30. Huang, M.; Gong, J.; Li, S.; Zhang, B.; Hao, Q. Study on hyperspectral time series and sensitive features for pine wood nematode disease. *Remote Sens. Technol. Appl.* **2012**, *27*, 954–960. [CrossRef]
31. Pan, J.; Xie, T.; You, C.; Xia, X. Dynamic Analysis of Early Stage Pine Wilt Disease in *Pinus massoniana* Using Ground-level Hyperspectral Imaging. *Forest Sci.* **2023**, *69*, 529–537. [CrossRef]
32. Carter, G.A.; Miller, R.L. Early detection of plant stress by digital imaging within narrow stress-sensitive wavebands. *Remote Sens. Environ.* **1994**, *50*, 295–302. [CrossRef]
33. Carter, G.A.; Cibula, W.G.; Miller, R.L. Narrow-band reflectance imagery compared with thermal imagery for early detection of plant stress. *J. Plant Physiol.* **1996**, *148*, 515–522. [CrossRef]
34. Jung, K.Y.; Park, J.K. Analysis of vegetation infection information using unmanned aerial vehicle with optical sensor. *Sensor Mater.* **2019**, *31*, 3319–3326. [CrossRef]
35. Huang, B. Monitoring *Bursaphelenchus xylophilus* with multispectrum camera in UAV. *Guangxi For. Sci.* **2020**, *49*, 380–384. [CrossRef]
36. Iordache, M.-D.; Mantas, V.; Baltazar, E.; Pauly, K.; Lewyckyj, N. A machine learning approach to detecting pine wilt disease using airborne spectral imagery. *Remote Sens.* **2020**, *12*, 2280. [CrossRef]
37. Liu, W.; Xie, Z.; Du, J.; Li, Y.; Long, Y.; Lan, Y.; Liu, T.; Sun, S.; Zhao, J. Early Detection of Pine Wilt Disease Based on UAV Reconstructed Hyperspectral Image. *Front. Plant Sci.* **2024**, *15*, 1453761. [CrossRef]
38. Zeng, Q.; Pu, Y.; Xiao, Y.; Yang, S.; Yang, Y.; Wang, X.; Xie, T.; Man, J.; Jia, Y. Early monitoring of southern Sichuan epidemic wood forest area based on UAV hyperspectral. *Sichuan For. Sci. Technol.* **2024**, *45*, 115–122.
39. Li, H.; Chen, L.; Yao, Z.; Li, N.; Long, L.; Zhang, X. Intelligent Identification of Pine Wilt Disease Infected Individual Trees Using UAV-Based Hyperspectral Imagery. *Remote Sens.* **2023**, *15*, 3295. [CrossRef]
40. Wu, W.; Zhang, Z.; Zheng, L.; Han, C.; Wang, X.; Xu, J.; Wang, X. Research progress on the early monitoring of pine wilt disease using hyperspectral techniques. *Sensors* **2020**, *20*, 3729. [CrossRef]
41. Duan, G. Derivation of the Arnon formula for chlorophyll content determination. *Plant Physiol. Commun.* **1992**, *3*, 221. [CrossRef]
42. Cubert-GmbH Hyperspectral Firefleye X20P. Available online: http://cubert-gmbh.de/ (accessed on 15 October 2020).
43. Wang, Y.; Wang, Y. Application Analysis of UAV Remote Sensing Technology in Forestry Resource Survey and Monitoring. *Agric. Technol.* **2018**, *38*, 167.
44. Yu, R.; Huo, L.; Huang, H.; Yuan, Y.; Gao, B.; Liu, Y.; Yu, L.; Li, H.; Yang, L.; Ren, L.; et al. Early Detection of Pine Wilt Disease Tree Candidates Using Time-Series of Spectral Signatures. *Front. Plant Sci.* **2022**, *13*, 1000093. [CrossRef]
45. Li, K.; Yang, S. Image smoothing and denoising based on the Savitzky–Golay algorithm. *Data Acquis. Process.* **2010**, *25*, 72–74. [CrossRef]
46. Kim, S.-R.; Lee, W.-K.; Lim, C.-H.; Kim, M.; Kafatos, M.C.; Lee, S.-H.; Lee, S.-S. Hyperspectral analysis of pine wilt disease to determine an optimal detection index. *Forests* **2018**, *9*, 115. [CrossRef]
47. Li, N.; Huo, L.; Zhang, X. Classification of pine wilt disease at different infection stages by diagnostic hyperspectral bands. *Ecol. Indic.* **2022**, *142*, 109198. [CrossRef]
48. Datt, B. Visible/near infrared reflectance and chlorophyll content in Eucalyptus leaves. *Int. J. Remote Sens.* **1999**, *20*, 2741–2759. [CrossRef]
49. Blackburn, G.A. Spectral indices for estimating photosynthetic pigment concentrations: A test using senescent tree leaves. *Int. J. Remote Sens.* **1998**, *19*, 657–675. [CrossRef]
50. Hunt, E.R., Jr.; Rock, B.N. Detection of changes in leaf water content using near- and middle-infrared reflectances. *Remote Sens. Environ.* **1989**, *30*, 43–54. [CrossRef]
51. Gitelson, A.A.; Merzlyak, M.N.; Chivkunova, O.B. Optical properties and nondestructive estimation of anthocyanin content in plant leaves. *Photochem. Photobiol.* **2001**, *74*, 38–45. [CrossRef]
52. Ashourloo, D.; Mobasheri, M.R.; Huete, A. Developing two spectral disease indices for detection of wheat leaf rust (*Puccinia triticina*). *Remote Sens.* **2014**, *6*, 4723–4740. [CrossRef]
53. Gamon, J.; Penuelas, J.; Field, C. A narrow-waveband spectral index that tracks diurnal changes in photosynthetic efficiency. *Remote Sens. Environ.* **1992**, *41*, 35–44. [CrossRef]
54. Penuelas, J.; Pinol, J.; Ogaya, R.; Filella, I. Estimation of plant water concentration by the reflectance water index WI (R900/R970). *Int. J. Remote Sens.* **1997**, *18*, 2869–2875. [CrossRef]
55. Hardisky, M.A.; Smart, R.M.; Klemas, V. Seasonal spectral characteristics and aboveground biomass of the tidal marsh plant, *Spartina alterniflora*. *Photogramm. Eng. Remote Sens.* **1983**, *49*, 85–92.
56. Raj, R.; Walker, J.P.; Vinod, V.; Pingale, R.; Naik, B.; Jagarlapudi, A. Leaf water content estimation using top-of-canopy airborne hyperspectral data. *Int. J. Appl. Earth Observ. Geoinf.* **2021**, *102*, 104024. [CrossRef]
57. Liu, Q.; Qu, Z.; Hu, X.; Bai, Y.; Yang, W.; Yang, Y.; Bian, J.; Zhang, D.; Shi, L. Combining UAV remote sensing data to estimate daily-scale crop water stress index: Enhancing diagnostic temporal representativeness. *Agric. Water Manag.* **2024**, *305*, 109130. [CrossRef]

58. Liu, S.; Wang, Q.; Wei, W.; Tang, Q.; Liu, L.; He, H.; Lu, J. Recognition of pine wilt disease trees in high-resolution images based on multi-feature analysis. *Green Sci. Technol.* **2021**, *23*, 237–240. [CrossRef]
59. Li, H.; Yu, L.; Zhan, Z.; Chi, S.; Ren, L.; Luo, Y. Effects of stand and landscape-level factors on the occurrence of pine wilt disease: A case study of pine forests in Weihai, Shandong. *J. Environ. Entomol.* **2024**, *46*, 616–624.
60. Luo, J.; Yang, Y.; Shi, B. Two-dimensional Otsu multi-threshold image segmentation based on improved adaptive differential evolution algorithm. *Electron. Info Tech.* **2019**, *41*, 2017–2024. [CrossRef]
61. Mohamed, A.; Reda, M.; Mohamed, A. A new fusion of whale optimizer algorithm with Kapur's entropy for multi-threshold image segmentation: Analysis and validations. *Artif. Intell. Rev.* **2022**, *55*, 71. [CrossRef]
62. Xu, M.; Chen, S.; Gao, X.; Ye, Q.; Ke, Y.; Huo, C.; Liu, X. Research on fast multi-threshold image segmentation technique using histogram analysis. *Electronics* **2023**, *12*, 3785. [CrossRef]
63. Ding, G.; Huang, S. Image retrieval combining multi-feature and linear discriminant analysis. *Comput. Appl. Softw.* **2024**, *41*, 212–218.
64. Xie, C.; Qin, Y.; Zhang, K.; Wang, X. Pseudo 3D residual network based on minimum intra-class variance. *J. Comput. Appl. Res.* **2021**, *38*, 3801–3807. [CrossRef]
65. Li, J.; Wang, X.; Zhao, H.; Hu, X.; Zhong, Y. Detecting Pine Wilt Disease at the Pixel Level from High Spatial and Spectral Resolution UAV-Borne Imagery in Complex Forest Landscapes Using Deep One-Class Classification. *Int. J. Appl. Earth Obs. Geoinf.* **2022**, *112*, 102947. [CrossRef]
66. Xie, W.; Wang, H.; Liu, W.; Zang, H. Early-Stage Pine Wilt Disease Detection via Multi-Feature Fusion in UAV Imagery. *Forests* **2024**, *15*, 171. [CrossRef]
67. Xia, L.; Zhang, R.; Chen, L.; Li, L.; Yi, T.; Wen, Y.; Ding, C.; Xie, C. Evaluation of deep learning segmentation models for detection of pine wilt disease in unmanned aerial vehicle images. *Remote Sens.* **2021**, *13*, 3594. [CrossRef]
68. Tao, H.; Li, C.; Cheng, C.; Jiang, L.; Hu, H. Research progress on remote sensing monitoring of pine wilt disease–discolored pine trees. *J. Forest Sci. Res.* **2020**, *33*, 172–183. [CrossRef]
69. Li, N.; Huo, L.; Zhang, X. Using Only the Red-Edge Bands Is Sufficient to Detect Tree Stress: A Case Study on the Early Detection of PWD Using Hyperspectral Drone Images. *Comput. Electron. Agric.* **2024**, *217*, 108665. [CrossRef]
70. Zhang, X. Spectral feature enhancement-based hyperspectral image object recognition. *Infrared Technol.* **2010**, *32*, 717–722.
71. Zhang, K. Hyperspectral Image Classification Based on Separable Features. Ph.D. Thesis, Hefei University of Technology, Hefei, China, 2022.